Preparation of Spinel-Type Black Pigments Using Microwave-Assisted Calcination of Stainless Steel Dust: The Effect of Manganese Molar Content

Xiang Zhang [1,2], Yanghui Xu [1,2], Zhiqiao Li [1,3], Mengke Liu [1,2,*], Tianyu Du [1,2], Ruixiang He [1,2] and Guojun Ma [1,2,*]

1   Key Laboratory for Ferrous Metallurgy and Resources Utilization of Ministry of Education, Wuhan University of Science and Technology, Wuhan 430081, China; zx91@wust.edu.cn (X.Z.); xuyanghui@wust.edu.cn (Y.X.); lzq@wust.edu.cn (Z.L.); dty2021@wust.edu.cn (T.D.); 1669289301@wust.edu.cn (R.H.)
2   Hubei Provincial Key Laboratory of New Processes of Ironmaking and Steelmaking, Wuhan University of Science and Technology, Wuhan 430081, China
3   State Key Laboratory of Vanadium and Titanium Resources Comprehensive Utilization, Pangang Group Research Institute Co., Ltd., Panzhihua 617000, China
*   Correspondence: liumengke@wust.edu.cn (M.L.); gma@wust.edu.cn (G.M.)

Abstract: Stainless steel dust is rich in valuable metal elements including Fe, Cr, Ni and Mn, which can be utilized to prepare Fe–Cr–Ni–Mn series black pigments. Meanwhile, manganese can absorb the majority of the visible light wavelength range, which improves the color rendering performance of Fe–Cr–Ni–Mn series black pigments. However, the coloring mechanism of manganese in the above black pigments is not clear. Therefore, the effect of manganese oxide content on the preparation of spinel-type black pigments from microwave-assisted calcination of stainless steel dust was studied in this work. The results show that with the increase in MnO content in the raw mixture, the crystal plane spacing of black pigments increases from 0.2525 nm to 0.2535 nm, the grain size grows from 61.4619 nm to 79.7171 nm, and the lattice constant grows from 0.8377 to 0.8406 nm. Moreover, the band gap is decreased from 1.483 eV to 1.244 eV, the absorbance increases significantly and has a consistent absorbance in the visible range, and the L^*, a^* and b^* values reduce from 41.8, 0.6, 1.6 to 32.0, 1.0, 0.8, respectively. MnO can react with the spinel in stainless steel dust, forming Mn_3O_4, $MnCr_2O_4$ and $Ni(Fe,Cr)O_4$ in the system, with a regular polyhedral structure. The prepared pigments have excellent thermal stability at 1100 °C and good compatibility with transparent glazes, which can be adhered to the surface of ceramic tiles after calcination to demonstrate better compatibility as the content of MnO increases.

Keywords: stainless steel dust; ceramic pigment; manganese; microwave; coloring mechanism

1. Introduction

Stainless steel dust (SSD) is a by-product of the stainless steel smelting process that is high in transition metal elements such as Fe, Cr, Ni, and Mn. During the manufacturing process, around 18–33 kg of SSD can be emitted for every ton of crude stainless steel produced [1–3]. Currently, the treatment process of SSD is widely classified as solidification landfill treatment, pyrometallurgical treatment and hydrometallurgical treatment [4–6]. Despite the solidification, and that landfill treatment can stabilize the heavy metal elements in SSD and reduce leachate concentration below the limit, the valuable metals from SSD have not been effectively exploited [7]. Moreover, hydrometallurgy and pyrometallurgy treatment processes also have some disadvantages, such as complicated process flow, unstable metal recovery, high energy consumption and secondary pollutants [8–10].

To achieve the harmless treatment of industrial solid waste, the processing of transition metal-enriched industrial solid waste into black ceramic pigments has gained favor among

scholars [11–14]. According to the above ideology, and based on the composition features of SSD, the use of SSD to prepare black ceramic pigments was proposed to avoid the drawbacks of traditional treatment processes and achieve high value-added utilization and harmless treatment of SSD [15,16]. Typically, industrial solid wastes are used to make three types of Co-free black ceramic pigment: Fe–Cr, Fe–Cr–Ni, and Fe–Cr–Ni–Mn series. The preparation of the first two series of pigments by SSD has been studied and the proportion of SSD in raw materials is higher than 50% [17,18]. Furthermore, according to the color rendering principle of black ceramic pigments, which states that the more transition metal element species are enriched, the wider the range of visible light that can be absorbed by the ion leap class and the stronger the absorbance. As a result, the color rendering properties of Fe–Cr–Ni–Mn series spinel-type black ceramic pigments are optimal among the three series [18]. Manganese may exist in various oxidation states and it may potentially exert its impact on black ceramic pigments via multiple reaction mechanisms, such as redox reactions and coordination bonding. The complexity of these reaction mechanisms make it more challenging to comprehend how manganese affects the properties of black ceramic pigments. Therefore, the effect of Mn on Fe–Cr–Ni–Mn series black ceramic pigments prepared by SSD needs to be investigated.

Additionally, the solid-state reaction synthesis method is widely employed in the preparation of black ceramic pigments from industrial solid wastes [19]. However, raising the raw materials' temperature using the conventional heating method takes a long time. Consequently, a significant temperature gradient arises between the interior and exterior, rendering it prone to excessive grain growth and over-sintering [20]. In contrast, microwave heating as a low-energy consumption alternative, offers the benefits of selective heating. Moreover, it effectively addresses the issue of a "cold center" and ensures that materials are heated quickly and uniformly [21]. The ability of the transition elements to absorb microwaves is good. Thus, manganese will also impact the heating behavior of raw materials.

In this study, the effects of manganese molar content in the raw material on the preparation and properties of pigments were investigated by gradually adding MnO to adjust the molar ratios of Fe, Cr, Ni, and Mn in the raw materials. By using XRD, FTIR, and SEM, the prepared pigment's crystal structure, phase composition and coloring mechanism were investigated. The findings may provide theoretical and experimental grounds for the harmless utilization of SSD.

2. Experiment

2.1. Raw Material

The SSD was collected from a stainless steel plant located in southeast China. The chemical reagents: Cr_2O_3, NiO and MnO (analytically pure) were from Sinopharm, and both ceramic paste and common transparent glaze powder were procured from a ceramic factory in southern China. Table 1 displays the chemical composition of the SSD, ceramic paste and the common transparent glaze powders. From Table 1, it is demonstrated that the SSD has a comparatively high amount of Cr_2O_3 and Fe_2O_3 (10.68 wt.% and 69.60 wt.%, separately). Al_2O_3 and SiO_2 make up the majority of ingredients in the ceramic paste (20.29 wt.% and 66.41 wt.%, respectively); meanwhile, transparent glazes have a higher percentage of Al_2O_3, SiO_2 and CaO (11.14 wt.%, 52.38 wt.% and 11.13 wt.%, respectively).

The XRD patterns depicted in Figure 1 reveal that the SSD is mostly composed of Fe_2O_3, SiO_2, and spinel phases. The ceramic paste is made up of SiO_2 and $Ca(Al_2Si_2O_8)$. Moreover, the common transparent glaze is mainly composed of SiO_2, $(Na,Ca)Al(Si,Al)O_3$, $KAlSiO_3$ and ZnO. Meanwhile, the particle size of SSD was analyzed by a laser particle size analyzer (Matersizer 2000, Malven, UK, test range: 0.02–2000 μm). As can be seen from Figure 2, the particle size distribution of SSD is mainly centralized in the range of 1–10 μm, and the overall particle size plot is normally distributed.

Table 1. Chemical composition of the raw materials (wt.%).

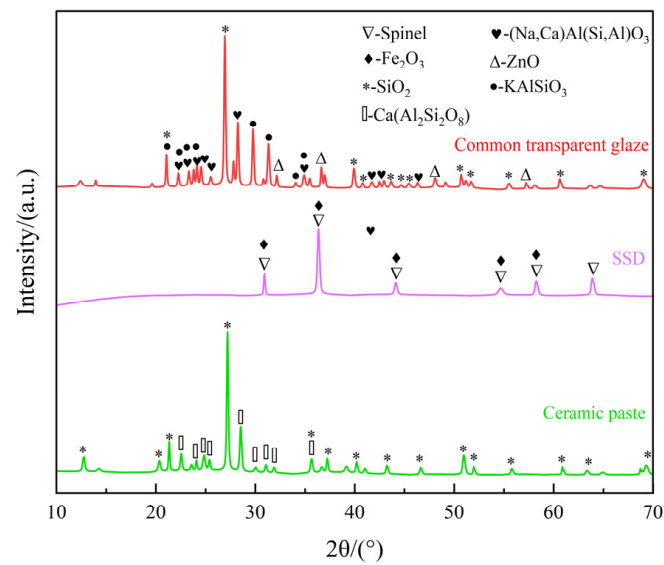| Composition	SSD	Ceramic Paste	Common Transparent Glaze
Al_2O_3	0.2	20.29	11.14
SiO_2	3.38	66.41	0.55
Fe_2O_3	69.60	0.55	0
CaO	5.21	1	11.13
MgO	0.55	1.35	1.80
ZnO	0.18	0	4.70
MnO	6.45	0	0
Cr_2O_3	10.68	0	0
NiO	1.03	0	0
K_2O	0	1.01	1.62
Na_2O	0	2.82	2.07
BaO	0	0	2.96
B_2O_3	0	0	0
LOI	0	0	11.36

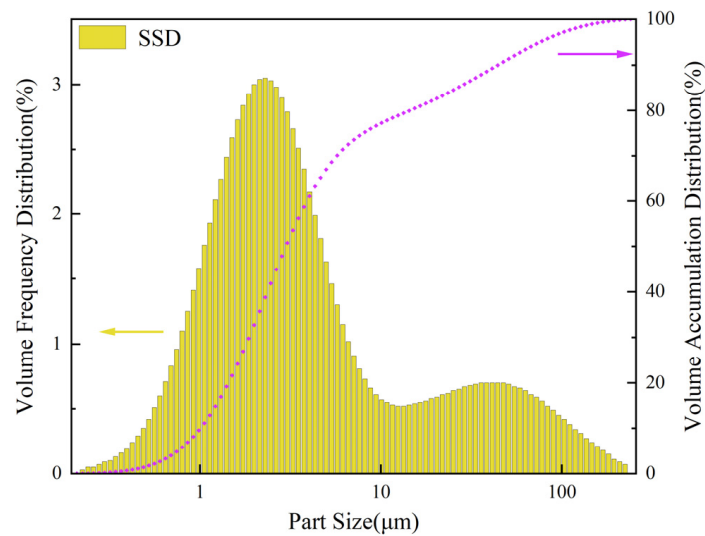**Figure 1.** XRD patterns of the SSD, the ceramic paste and the common transparent glaze.

Figure 2. Particle size distribution of SSD.

2.2. Process of Preparing Black Ceramic Pigments

At first, the raw mixtures with different Fe/Cr/Ni/Mn molar ratios (as shown in Table 2) were prepared by adding Cr_2O_3, NiO, and MnO to SSD individually. The raw mixtures were dried at 100 °C for 180 min to remove moisture. Thereafter, about 30 g of the raw mixture was placed in an alumina crucible and placed inside a microwave furnace (HUAE, HY-QS3016, Changsha, China). The microwave power was set at 2000 W and the heating rate was 50 °C/min. Then, the raw mixture was heated to 900 °C and maintained for 30 min in an air atmosphere. After the holding period, the crucible was immediately removed from the chamber and cooled to room temperature by air cooling. The pigment samples were then crushed to less than 200 mesh and stored under dry conditions for further use.

Table 2. Raw mixtures with different Fe/Cr/Ni/Mn molar ratios.

Sample	Fe/Cr/Ni/Mn Molar Ratio	$Fe_2O_3/Cr_2O_3/NiO/MnO$ Molar Ratio
S1	1:1:1:0.25	0.5:0.5:1:0.25
S2	1:1:1:0.5	0.5:0.5:1:0.5
S3	1:1:1:0.75	0.5:0.5:1:0.75
S4	1:1:1:1	0.5:0.5:1:1
S5	1:1:1:1.25	0.5:0.5:1:1.25
S6	1:1:1:1.5	0.5:0.5:1:1.5

2.3. Stability Test

The thermal stability of the pigment samples was tested by thermogravimetric analysis (NETZSCH, STA449C, Waldkraiburg, German) in an air atmosphere with a flow rate of 50 mL/min and a temperature ramp of 10 °C/min. The temperature range for the TG curves was from room temperature to 1200 °C.

The chemical stability of pigment samples, particularly their resistance to acid and alkali, was evaluated in accordance with GB/T 5211.5-2008 [17]. The following is the description of the method. Three test tubes containing 0.500 g of pigment samples were filled with 20 mL of deionized water, 2 wt.% hydrochloric acid solution and 2 wt.% sodium hydroxide solution separately. Afterward, the test tubes were violently shaken for 5 min to achieve thorough mixing. The suspensions in the test tubes were then individually filtered to extract the filtrate and the filter cake. Thereafter, the filtrates were transferred into cuvettes and the filter cakes were dried. Finally, both filter cake and cuvette underwent assessment for discoloration and staining, respectively.

2.4. Application of Pigments in Ceramic Glaze Preparation

A total of 4 g of ceramic paste and 2 g of deionized water were compacted into a cylindrical green compact using a tablet press machine with a pressure of 15 MPa and a molding time of 2 min. The ceramic green compacts were set inside a muffle furnace (SX2-10-13) on an alumina gasket, preheated for 30 min at 600 °C with a heating rate of 8 °C/min and then cooled by furnace-cooling.

To obtain black glaze slips, the various pigment samples were mixed with common transparent ceramic glaze powders and deionized water at a weight ratio of 0.05:1:1 individually. Meanwhile, a control glaze slip without pigments was set to evaluate the coloring performance of pigments.

Finally, immersion glazing was used to glaze the surfaces of the preheated green compacts. The glazed sample was then sintered for 30 min at 1200 °C (heating rate of 8 °C/min) to obtain ceramic tiles with pigmented surfaces. As Figure 3 illustrates, all calcining and cooling procedures were carried out in an air atmosphere.
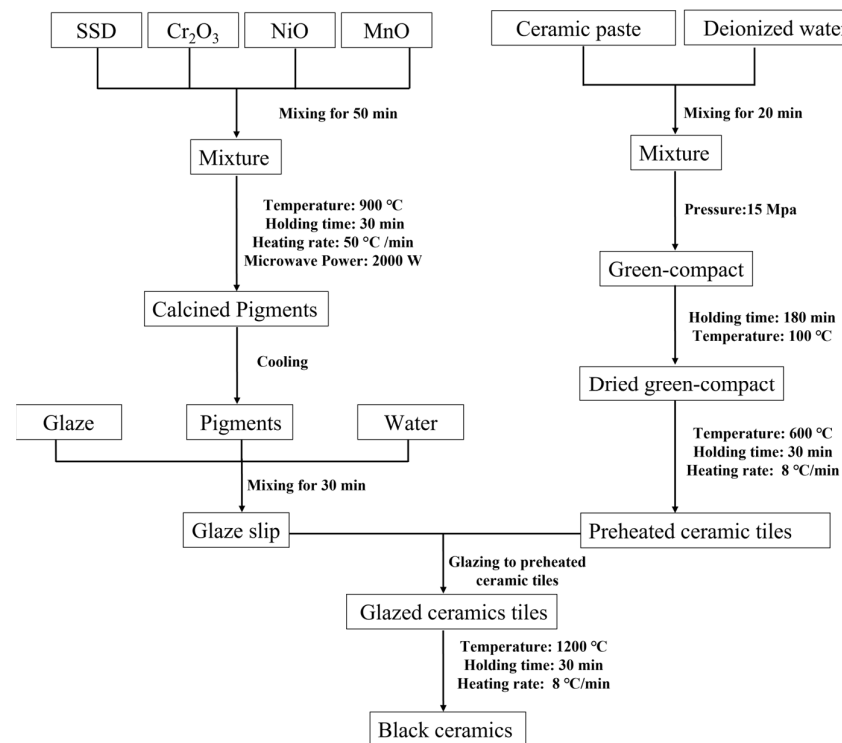
Figure 3. Flow chart of black ceramic preparation.

2.5. Characterizations

The chemical compositions of the SSD, the ceramic paste and the common transparent glaze powders were examined by using ICP-AES, (Thermo Elemental, IRIS Advantage ER/S, Waltham, MA, USA).

The phases and crystal structure of the SSD, the ceramic paste, the common transparent glaze and the prepared pigments were analyzed by using XRD (PANalytical, X'Pert PRO, Almelo, The Netherlands) with a Cu target Kα radiation source, a tube voltage of 40 kV, a tube current of 40 mA, a 2θ angle scanning angle range of 10°–70°, and a scanning rate of 2°/min.

The average crystallite sizes of pigment samples were obtained by applying the analytical results of the aforementioned XRD in conjunction with the computational method of Williamson–Hall (W-H), as shown in Equations (1)–(5).

$$\beta_T = \beta D + \beta \varepsilon \tag{1}$$

where β_T denotes the total broadening and includes the contributions from the broadening caused by crystallite size (β_D) and the broadening caused by micro-strain (β_ε).

According to the Scherer equation, as shown in Equation (2), it is evident that the crystallite size can be determined.

$$D = 0.89\lambda / \beta D \cos\theta \tag{2}$$

where D represents the crystallite size (nm), λ denotes the wavelength of X-ray (0.15406 nm), θ stands for the Bragg diffraction angle (°), ε stands for stress.

Likewise, the broadening of XRD diffraction peaks due to micro-strain is indicated as:

$$\beta \varepsilon = 4\varepsilon \tan\theta \tag{3}$$

By incorporating Equations (2) and (3) into Equation (1), Equation (4) can be derived, enabling the subsequent calculation of the average crystallite size (D) for the different pigment samples.

$$D = 0.89\lambda / (\beta_T \cos\theta - 4\varepsilon \sin\theta) \tag{4}$$

The crystal plane spacing (d) between grains contained in different pigment samples can be determined by the Bragg equation shown in Equation (5).

$$d = \lambda / 2 \sin \theta \tag{5}$$

Based on the calculated corresponding crystal plane spacing d, the lattice constant of the grains can be computed using Equation (6). In the equation, h, k and l are the Miller indices of crystal planes, while a, b, and c represent the lattice constants of the grains.

$$1/d^2 = h^2/a^2 + k/b^2 + l/c^2 \tag{6}$$

A FTIR spectrometer (Thermo Scientific, Nicolet-is50, Waltham, CA, USA) was used to analyze the infrared reflectance spectra of the prepared pigment samples in the range of 400–4000 cm^{-1} with the KBr pressure method. Furthermore, the diffuse reflectance spectra of pigment samples were also measured using a UV–Vis spectrophotometer (Shimadzu, UV-2600, Kyoto, Japan) at a wavelength range of 200–800 nm with $BaSO_4$ as the substrate and adopting the integrating sphere diffuse reflection method. The band gaps (E_g) of pigment samples were calculated using the Kubelka–Munk equation via the Tauc plot method [22], as demonstrated in Equation (7).

$$F(R) = (1 - R^2)/2R \tag{7}$$

where R signifies the reflectance of the pigment sample at a specific wavelength.

The relationship curves of $[F(R) hv]^{1/2}$ and hv can be obtained (h stands for Planck's constant 4.135×10^{-15} eV·s, v represents the frequency of light), then a tangent line is made to the X-axis through the linear main part of the curve and intersects with the X-axis, and the intercept values obtained are the band gap of the different pigments [23].

The microstructure and micro-constitution of the pigment samples were examined using a field emission scanning electron microscope (FEI, Nova NanoSEM400, Hillsboro, OR, USA) in conjunction with energy dispersive X-ray spectrometry (Oxford, PentaFET-X3, UK, Oxford). The chromaticity values of the pigment samples, including L^*, a^*, and b^* values were tested using a portable colorimeter (3 nh, TS7010, Shenzhen, China). The L^*, a^*, and b^* values correspond to color models developed by the International Commission on Illumination (CIE). Within the system, the L^* value indicates the lightness or darkness of a color on a scale ranging from white ($L^* = 100$) to black ($L^* = 0$). The a^* and b^* values signify the color scale from green ($-a^*$) to red ($+a^*$) and from blue ($-b^*$) to yellow ($+b^*$), respectively. The corresponding color saturation value C^* can be calculated from a^* and b^* values of test pigment samples, as shown in Equation (8) [24].

$$C* = [(a*)^2] + [(b*)^2]^{1/2} \tag{8}$$

Color saturation indicates the color purity of the pigment samples, and the closer the L^*, a^*, b^* and C^* values of the black ceramic pigments are to 0, the better the black color rendering performance of the pigments [25].
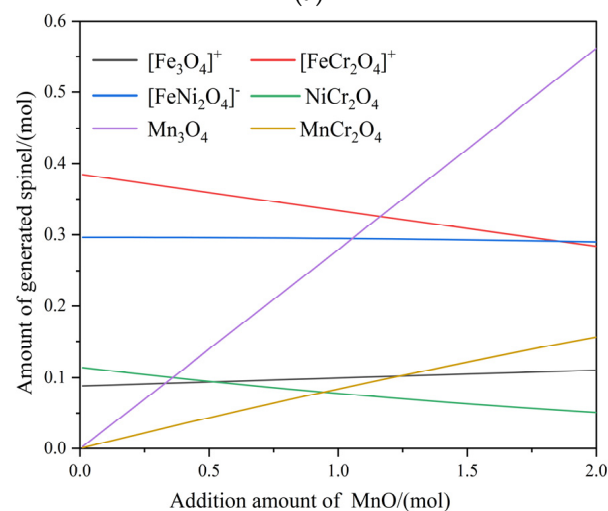
3. Results and Analysis

3.1. Thermodynamic Analysis of the Fe_2O_3–Cr_2O_3–NiO–MnO Reaction System

Figure 4 displays the thermodynamic calculation results of the Fe_2O_3–Cr_2O_3–NiO–MnO reaction system (the Fe/Cr/Ni molar ratio is 1:1:1) at different MnO additions applying the Equilib module of FactSage 8.1. The calculations were conducted at a calcination temperature of 900 °C in an air atmosphere with an oxygen partial pressure of 0.21 standard atmospheres. Meanwhile, the impurity elements in SSD were not taken into account, and only the interactions among the four metal oxides (Fe_2O_3, Cr_2O_3, NiO and MnO) were considered. As shown in Figure 4a, when MnO is not added, the reaction product contains only spinel. With the increase in MnO after addition, the growth rate

of spinel content is slightly faster than that of NiO. Combined with the results shown in Figure 4b, it indicates that in addition to the substitution of Mn^{2+} for the dot position occupied by Ni^{2+}, part of MnO will be oxidized to spinel Mn_3O_4. More precisely, the content of $NiCr_2O_4$ in the system gradually decreases while $MnCr_2O_4$ shows an increasing trend, which indicates that Mn^{2+} will occupy the Ni^{2+} position in the original $NiCr_2O_4$ and generate the $MnCr_2O_4$ phase.
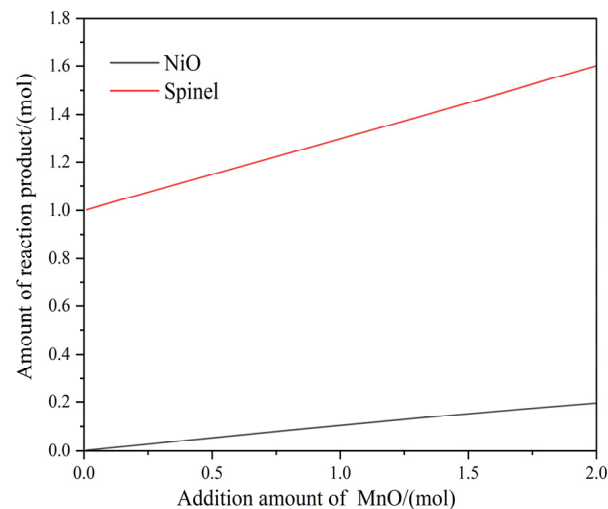
(a)

(b)

Figure 4. Thermodynamic calculation results of the Fe_2O_3–Cr_2O_3–NiO–MnO reaction system. (**a**) Amount of different reaction products; (**b**) Amount of different spinels.

3.2. Thermal Stability of the Raw Mixture

Figure 5 shows the TG–DSC curves of S4 raw mixture from room temperature to 1200 °C. The TG curve decrease is firstly caused by the volatilization of free and bound water. The subsequent rises in the TG curve from about 100 °C to 600 °C with the exothermic DSC curve is due to the oxidation of metal elements.

The TG curve shows an obvious declining peak at about 600 °C, which is attributed to the decomposition of Ni_2O_3 produced after the oxidation of NiO [26]. During the period of the temperature climbing from 700 °C to 900 °C, the results of TG–DSC curves suggest that the solid solution reaction in the system has been carried out and gradually occupies a dominant position at this stage. When the reaction temperature exceeds 900 °C, the DSC curve decreases rapidly. The situation primarily arises due to the elevation in vapor pressure of Cr_2O_3, resulting in the decomposition of spinel [27]. Therefore, a

reasonable calcination temperature is conducive to the complete structure of spinel and high crystallization strength of the pigments.
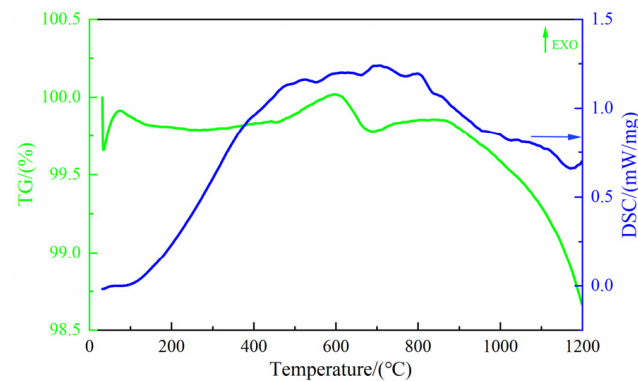

Figure 5. TG–DSC curve of the raw mixture S4.

Meanwhile, Table 3 shows the possible reactions in the system calculated by Fact-Sage8.1. It is found that MnO is more easily oxidized to Mn_3O_4 in an air atmosphere, and this aligns with the previous analysis.

Table 3. Possible reactions in the feedstock system.

Reactions	$\Delta_r G_m{}^\theta = \Delta H - T\Delta S (J)$
$4FeO(s) + O_2(g) = 2Fe_2O_3(s)$	$-573{,}655 + 243.35T$ (273–1773 K)
$4Fe_3O_4(s) + O_2(g) = 6Fe_2O_3(s)$	$-488{,}333 + 270.82T$ (273–1773 K)
$4MnO(s) + O_2(g) = 2Mn_2O_3(s)$	$-373{,}811 + 226.71T$ (273–1773 K)
$6MnO(s) + O_2(g) = 2Mn_3O_4(s)$	$-458{,}953 + 248.54T$ (273–1773 K)
$3MnO(s) + 3Fe_2O_3(g) = 2Fe_3O_4(s) + Mn_3O_4(s)$	$14{,}602 - 11.072T$ (273–1773 K)
$2MnO(s) + O_2(g) = 2MnO_2(s)$	$-258{,}742 + 205.37T$ (273–1773 K)
$FeO(s) + Fe_2O_3(s) = Fe_3O_4(s)$	$-21{,}331 - 6.8679T$ (273–1773 K)
$FeO(s) + Cr_2O_3(s) = FeCr_2O_4(s)$	$-70{,}814 + 15.81T$ (273–1773 K)
$NiO(s) + Fe_2O_3(s) = NiFe_2O_4(s)$	$-22{,}149 + 7.7441T$ (273–1773 K)
$NiO(s) + Cr_2O_3(s) = NiCr_2O_4(s)$	$-9687 - 1.1389T$ (273–1773 K)
$MnO(s) + Fe_2O_3(s) = MnFe_2O_4(s)$	$-15{,}602 - 5.5925T$ (273–973 K) $-24{,}233 + 3.7215T$ (973–1773 K)
$4FeO(s) + O_2(g) + 2NiO(s) = 2NiFe_2O_4(s)$	$-617{,}952 + 258.84T$ (273–1773 K)
$4Fe_3O_4(s) + O_2(g) + 6NiO(s) = 6NiFe_2O_4(s)$	$-621{,}224 + 317.28T$ (273–1773 K)

3.3. XRD Analysis and Crystal Structure of the Prepared Pigments

Figure 6 shows the XRD patterns of the S1–S6 samples. Upon the addition of a small quantity of MnO, the primary phase in the S1 sample consists of a spinel phase with a small amount of NiO. This indicates that the reaction system has undergone the spinel transformation reaction at 900 °C. As the MnO content increases, the diffraction peak associated with the spinel phase gradually becomes sharper and has a smaller half-peak width, and the crystallinity of the spinel phase is increased. The intensity of NiO also rises proportionally with the increase in MnO, which is consistent with the results of thermodynamic analysis. Meanwhile, as Figure 6 illustrates, the characteristic diffraction peaks of the spinel phase gradually shifted to the small angle direction with the increase in MnO content. This suggests that the doping of MnO caused the spinel phase to exhibit an increasing trend of grain plane spacing and lattice constant, which leads to lattice expansion, stress increases, and average grain size increases.
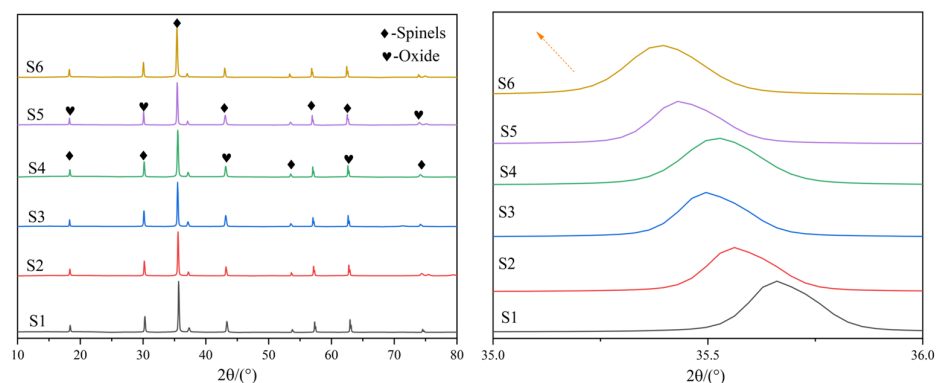
Figure 6. XRD patterns of prepared pigment samples.

Based on the XRD data, the lattice parameters and average grain size of pigments with different MnO additions were calculated using the Williamson–Hall (W–H) method and Bragg's formula, as shown in Table 4. Since spinel belongs to the cubic crystal system, its lattice constant $a = b = c$. It can be observed from Table 4 that the lattice constants of the prepared pigments are different from those of the single spinel phase.

Table 4. Lattice parameters and average grain size of the spinel phases.

Sample	$2\theta/(°)$	$d/(nm)$	$D/(nm)$	$a = b = c/(nm)$	ε	FWHM
S1	35.6607	0.2525	61.4619	0.8377	0.00101	0.19379
S2	35.5617	0.2523	67.8779	0.8366	0.00102	0.18042
S3	35.4957	0.2527	73.7168	0.8381	0.00111	0.18515
S4	35.5287	0.2526	74.5451	0.8378	0.00120	0.19273
S5	35.4297	0.2531	76.3250	0.8395	0.00154	0.18844
S6	35.3967	0.2535	79.7171	0.8406	0.00134	0.18425

The main reason for the above phenomenon is that most of the MnO is oxidized to Mn_3O_4, and Mn^{3+} (0.0645 nm) and Mn^{2+} (0.067 nm) are larger than Fe^{3+} (0.055 nm) and Cr^{3+} (0.0615 nm), leading to an increase in the average grain size [28]. At the same time, the gradual increase in stress also leads to distortion of the lattice. The stress is attributed to the incorporation of Mn^{2+} and Mn^{3+} into the lattice and alters the arrangement of atoms or ions in the crystal. As a result, stress concentrates in the vicinity of Mn^{2+} and Mn^{3+}, creating a localized stress field. This localized stress field extends to a larger range, causing an increase in internal stress that ultimately results in lattice distortion.

3.4. FTIR Analysis of the Prepared Pigments

The FTIR analysis results of the pigment samples (S1–S6) are depicted in Figure 7. It is determined from Figure 7 that all pigment samples exhibit eight similar absorption vibrational peaks, which are observed near 3422 cm^{-1}, 1610 cm^{-1}, 1579 cm^{-1}, 1370 cm^{-1}, 1080 cm^{-1}, 774 cm^{-1}, 610 cm^{-1} and 493 cm^{-1}, separately. The vibrational peak of the octahedral skeleton of MnO_6 appears at 760–900 cm^{-1}, which also indicates an oxidation of MnO in the raw material to Mn^{3+}, while participating in the spinel reaction, and occupying the tetrahedral position [27]. Meanwhile, the absorption peak at 610 cm^{-1} belongs to the bending and stretching vibration of the tetrahedra in the spinel phase. The absorption peak at 610 cm^{-1} in the infrared spectrum of the S4 sample is noticeably higher compared to other samples. This observation can be attributed to the presence of a higher concentration of tetrahedral complexes. Additionally, the majority of the added MnO exists in the Mn^{2+} state within the S4 sample. The strong absorption peak near 493 cm^{-1} corresponds to the octahedron, which has a broader absorption peak at its position due to its composition of multiple functional groups, including FeO_6 and CrO_6, and due to the fine grain size of the prepared pigment spinel phase, which will also lead to its broadening [29].
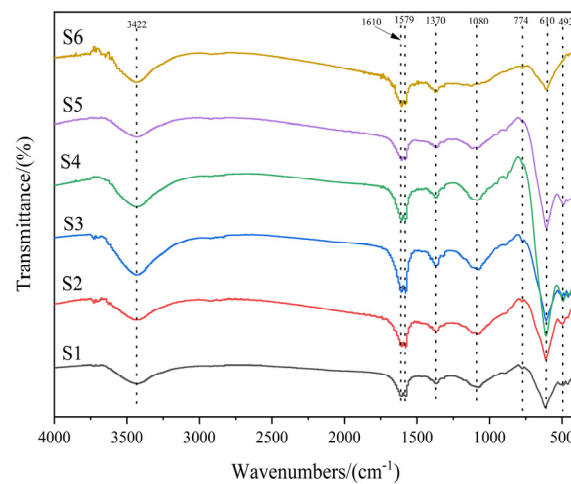
Figure 7. FTIR of pigment samples S1–S6.

3.5. SEM of the Prepared Pigments

Figure 8 shows the SEM–EDS photographs of prepared pigment samples with different MnO additions. As shown in Figure 8a–g, with the gradual addition of MnO, the particle size gradually increases, and most of them are spinels shaped like regular polyhedrals. At the same time, the irregular shape of the solid solution phase gradually reduces and disappears. Moreover, the surface morphology of pigment particles gradually changes to a regular geometry and becomes relatively consistent without obvious defects, which also indirectly indicates that the crystallinity gradually increases with the increase in MnO content. The micro-constitution analysis results show that the Mn content in spinel particles also increases.

Additionally, some pigment particles have a proclivity to agglomerate or fuse, resulting in the formation of lamellar particles with no distinct crystalline surface. This is because high temperature promotes the diffusion of atoms and ions, causing the migration of material from smaller particles to larger ones, further reducing the surface energy, van der Waals force, Coulomb force or chemical bonding cooperation of the particles, reducing the surface tension and capillary adsorption, making the surface energy reach a steady state. Furthermore, the pigment samples contain Fe_3O_4, $MnCr_2O_4$ and other weak magnetic substances. In the absence of an external magnetic field, these weakly magnetic materials attract one another, resulting in the magnetic dipole effect, which can also result in the above phenomenon [30].
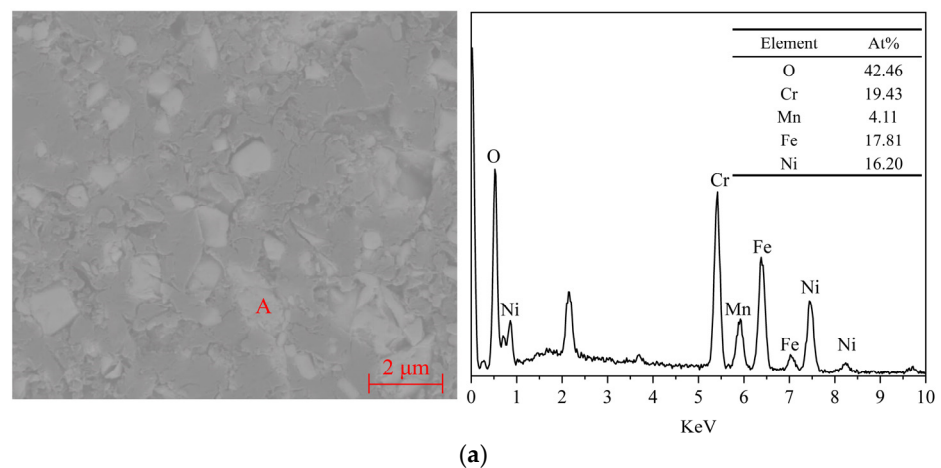

(a)

Figure 8. *Cont.*

Element	At%
O	30.71
Cr	25.07
Mn	10.72
Fe	16.22
Ni	17.28

(**b**)

Element	At%
O	44.25
Cr	16.18
Mn	11.01
Fe	15.40
Ni	13.16

(**c**)

Element	At%
O	35.20
Cr	15.18
Mn	13.42
Fe	14.28
Ni	21.92

(**d**)

Figure 8. *Cont.*

Element	At%
O	44.09
Cr	13.53
Mn	15.96
Fe	13.53
Ni	12.89

(**e**)

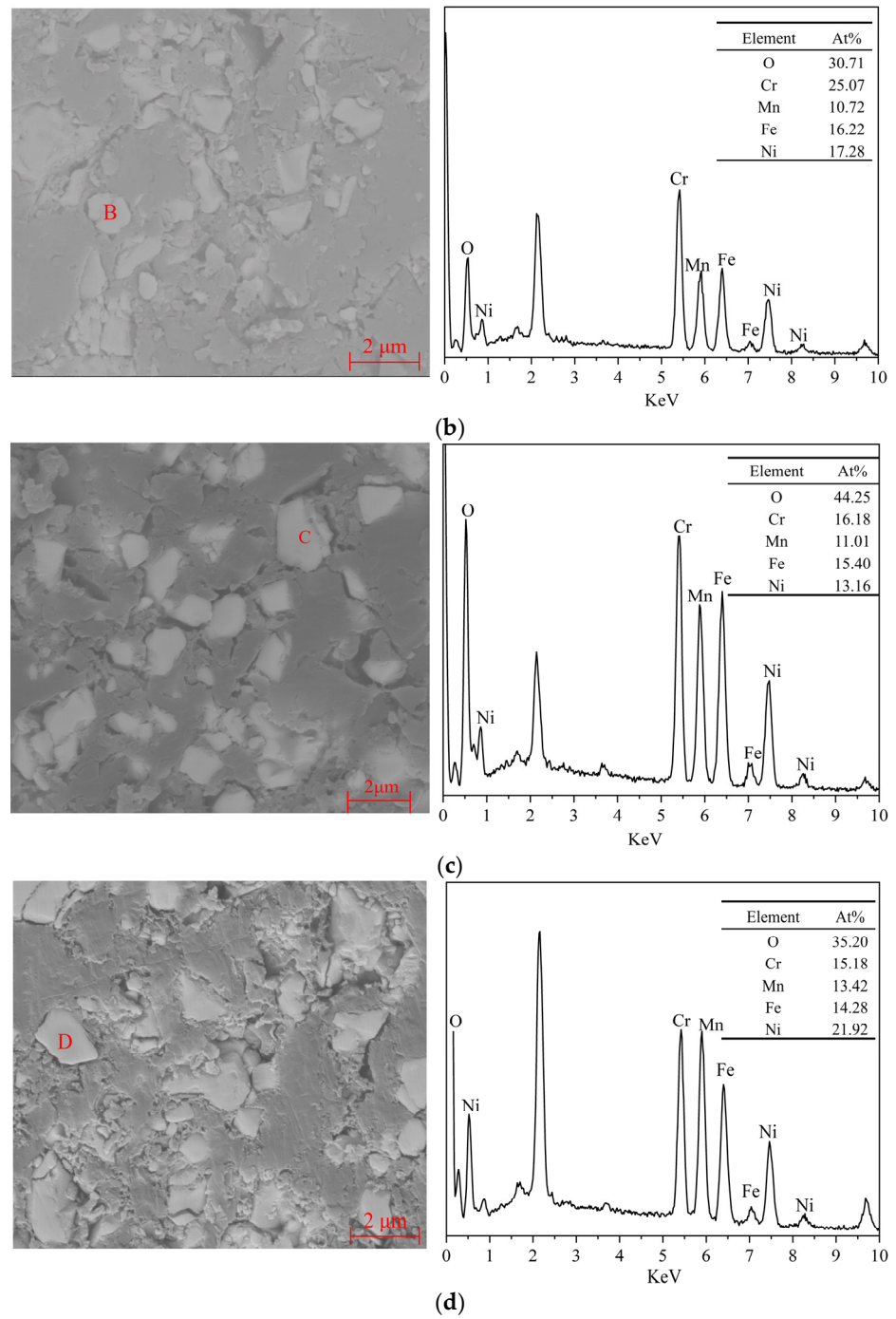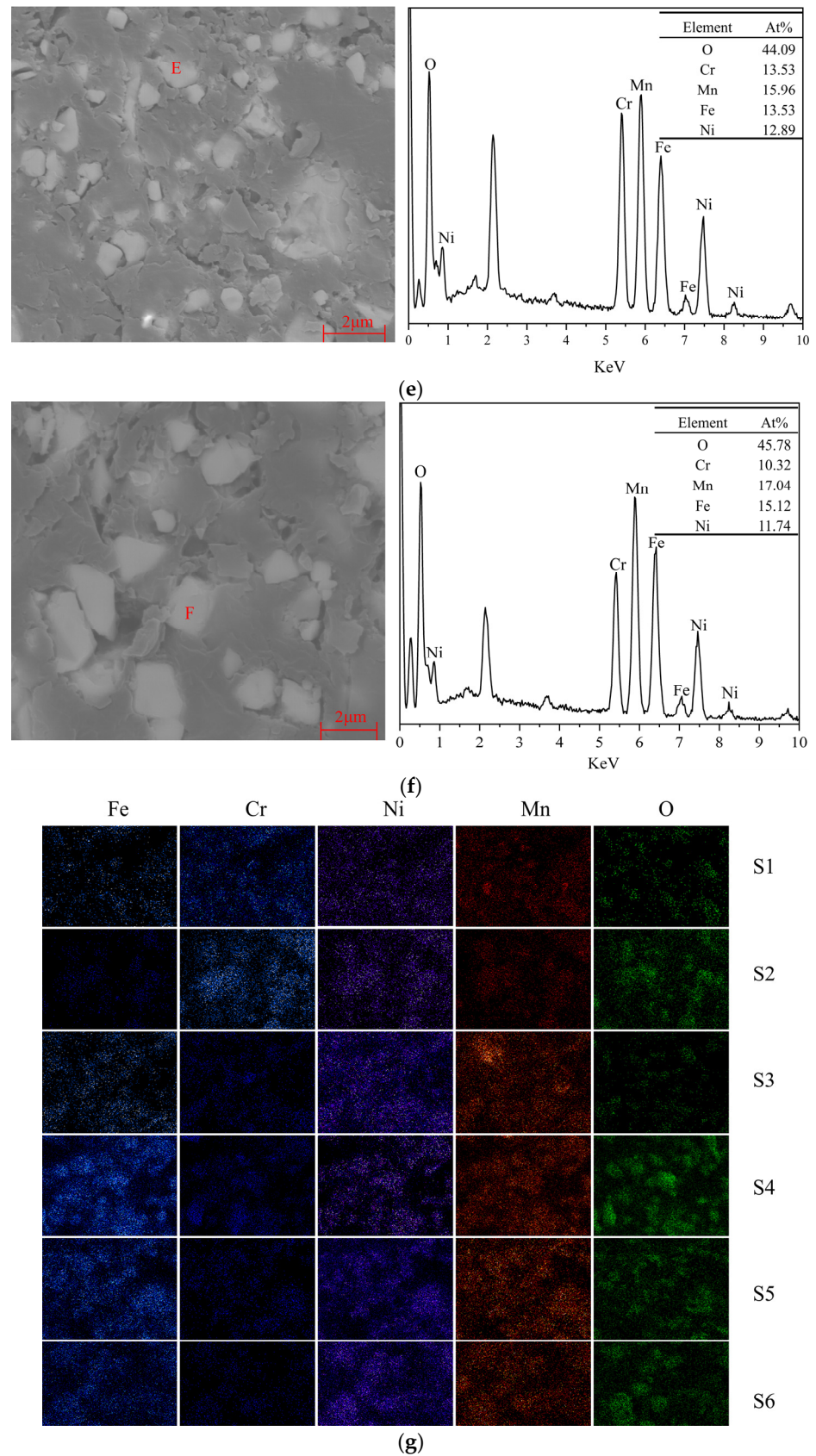| Element	At%
O	45.78
Cr	10.32
Mn	17.04
Fe	15.12
Ni	11.74

(**f**)

(**g**)

Figure 8. SEM–EDS of prepared ceramic pigments with different additions of MnO. (**a**) A point of S1 sample; (**b**) B point of S2 sample; (**c**) C point of S3 sample; (**d**) D point of S4 sample; (**e**) E point of S5 sample; (**f**) F point of S6 sample; (**g**) EDS-mapping of S1–S6 sample.

3.6. Optical Properties of the Prepared Pigments

The UV–Vis absorption spectra of pigment samples are shown in Figure 9. All of the pigment samples have an approximate level of linear absorption in the visible spectrum from 380–780 nm. This indicates that the pigment samples can uniformly absorb different wavelengths of visible light, resulting in the black of the pigment samples. The absorbance of the pigment samples increases simultaneously with the gradual increase in MnO addition in the raw materials.
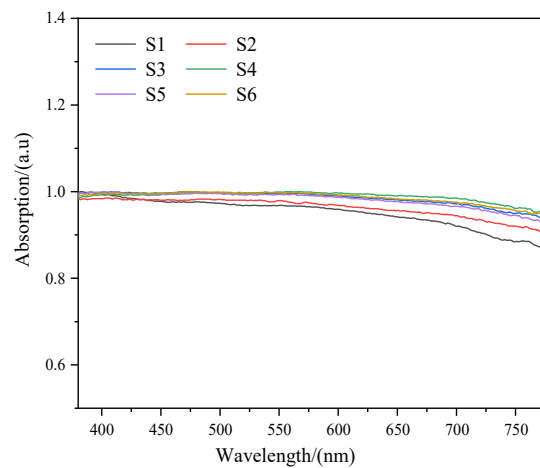

Figure 9. UV–Vis absorbance spectra of prepared ceramic pigments with different additions of MnO.

According to the crystal field theory, the Fe–Cr–Ni–Mn spinel pigments are colored because the transition metal elements they contain are in the ligand (ortho-spinel AB_2O_4, A tetrahedral, B octahedral), and are in the corresponding crystal field, and when exposed to light radiation the d-orbital electrons at lower energy levels absorb energy and jump to the excited state, undergoing a d–d electron transition [31]. This excitation process absorbs energy corresponding to the light energy in the visible range causing the pigment to show color [32].

Table 5 lists the transition types present in the visible band of Fe–Cr–Ni–Mn series black ceramic pigments and the visible range of the corresponding band that can be absorbed. It can be seen from Table 5 that the transition types present in the pigments cover all the wavelengths in the visible range, so that the pigments finally appear black. This absorption of a different frequency of light is attributed to the conversion between different energy levels of ions.

Table 5. The transition forms present in pigment samples and the corresponding absorption visible light range.

Element	Coordination Number	Transition Type	Absorption Band/nm	Reference
Ni (II)	4	2p (O^{2-})→3d (Ni^{3+})	340–370	[33]
Mn (II)	4	${}^4A_{2g} \rightarrow {}^4T_{1g}$ ${}^4A_{2g} \rightarrow {}^2T_{2g}$ ${}^6A_{1g} \rightarrow {}^4T_{1g}$ ${}^6A_{1g} \rightarrow {}^4T_{2g}$ ${}^6A_{1g} \rightarrow {}^4E_{g}$ ${}^6A_{1g} \rightarrow {}^4A_{1g}$	380–450	[34]
Cr (III)	6	${}^4A_{2g} \rightarrow {}^4T_{1g}$ ${}^4A_{2g} \rightarrow {}^2T_{2g}$	400–500	[35]
Ni (II)	6	${}^3A_{2g} \rightarrow {}^3T_{1g}$	420–480	[36]
Fe (III)	4	2p (O^{2-})→3d (Fe^{3+})	450–500	[37]
Fe (III)	6	2p (O^{2-})→3d (Fe^{3+})	500–700	[37]
Mn (II)	4	${}^4A_{2g} \rightarrow {}^2E_{g}$ ${}^4A_{2g} \rightarrow {}^4T_{1g}$	570–580	[38]

Table 5. *Cont.*

Element	Coordination Number	Transition Type	Absorption Band/nm	Reference
Mn (III)	6	$2p\ (O^{2-}) \to 3d\ (Mn^{3+})$	700–800	[39]
Cr (III)	6	${}^4A_{2g} \to {}^4T_{2g}$ ${}^4A_{2g} \to {}^2T_{1g}$ ${}^4A_{2g} \to {}^2E_g$	550–700	[40]
Fe (III)	6	${}^6A_{1g} \to {}^4T_{1g}$ ${}^6A_{1g} \to {}^4T_{2g}$	700	[41]

As the content of MnO increases, the absorbance of the pigment sample in visible light from 400 to 700 nm, which is mostly due to the spin allowed transitions ${}^4A_{2g} \to {}^4T_{1g}$ of Cr^{3+} in the octahedral position and $2p\ (O^{2-}) \to 3d\ (Fe^{3+})$ of Fe^{3+} in the octahedral position [35,37]. Mn^{3+} in the octahedral position spin-allowed $2p\ (O^{2-}) \to 3d\ (Mn^{3+})$ to increase in visible light from 700 to 780 nm, and the crystal symmetry was improved [39]. It results in an increase in absorbance by enhancing the electronic transitions within the material.

In order to present in more detail the effect of MnO on the color rendering properties of black pigments, the band gap of the pigment samples was calculated by the Kubelka–Munk formula, as shown in Figure 10. In S1–S6 pigment samples, the band gap of the pigment samples gradually decreases with the addition of MnO. The band gap of the S4 pigment sample is the smallest. This is due to the doping of manganese atoms and may lead to the overlap or crossover of energy bands, causing a change in energy band structure. Furthermore, in the close atomic radius and electronegativity of each transition metal, mutual substitution occurs, and the orbital hybridization effect increases. The hybridized orbitals have a more powerful bonding ability than the original orbitals of the hybridized participating atoms, their spatial orientation improves the spatial configuration of the produced bonds. This reduces the repulsive forces between each bond or atom and stabilizes the molecular structure, thus reducing the energy required to jump between the conduction and valence bands [42]. As a result, the band gap narrows.
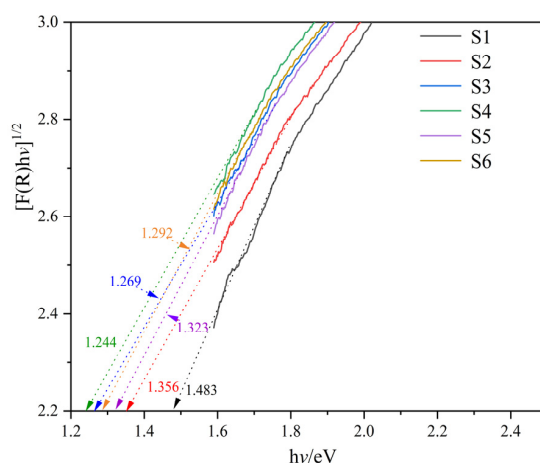

Figure 10. Band gaps of prepared pigment samples.

The chromaticity coordinates and chromaticity values in the chromaticity diagram were used to characterize and analyze the color rendering properties of the pigment samples with different MnO addition amounts, and the results are shown in Figure 11 and Table 6, respectively. It can be seen from Figure 11 that the color coordinates from S1 (0.3311, 0.3321) to S6 (0.3326, 0.3334) gradually become closer to the achromatic point O (0.3333, 0.3333), which indicates that the pigments have excellent coloring performance. In the S1–S4 pigment samples, the *L**, *a**, and *b** values decreased from 37.9, 0.3, −0.1 to 36.1, 0.2,

−0.1, respectively. However, the *L**, *a**, and *b** value of S5 and S6 pigment samples are slightly increased, as shown in Table 6.
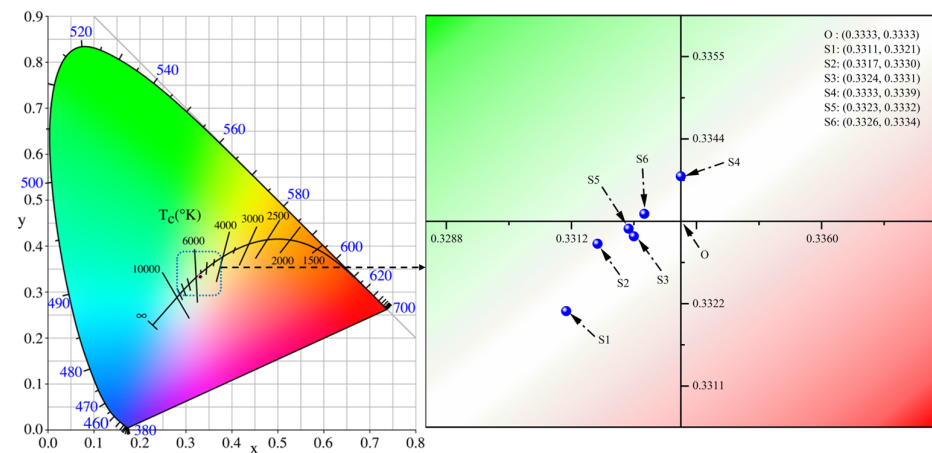

Figure 11. Chromaticity diagram of pigment samples prepared with S1–S6.

Table 6. The chromaticity values of prepared pigment samples.

Sample	*L**	*a**	*b**	*C**	Color Card
S1	37.9	0.3	−0.1	0.32	
S2	38.5	0.3	0.0	0.30	
S3	37.5	0.2	−0.1	0.22	
S4	36.1	0.2	−0.1	0.22	
S5	37.2	0.3	−0.1	0.32	
S6	37.3	0.2	−0.2	0.28	

3.7. Stability Testing of the Prepared Pigment Samples

TG curves of the pigment samples from room temperature to 1200 °C, are shown in Figure 12. The curve shows an almost horizontal straight line from room temperature to 1200 °C except for the S2 pigment samples, which may be due to spinel phase decomposition for S2 pigment samples. Among them, S4 has the best thermal stability. The tests above show that Fe–Cr–Ni–Mn series of black ceramic pigments produced using SSD have excellent thermal stability of less than 1200 °C.
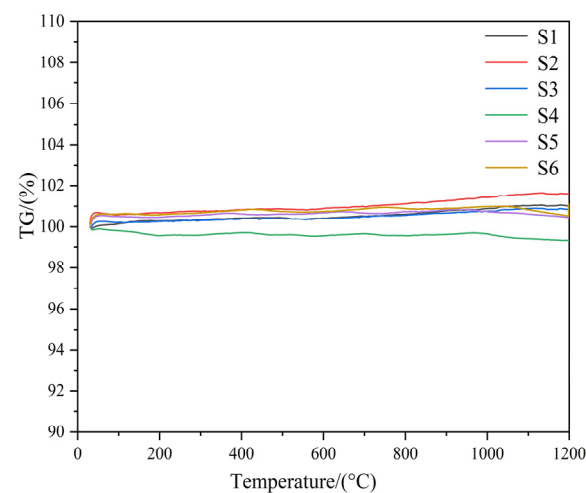

Figure 12. TG curve of prepared pigment samples.

In this experiment, GB/T 5211.5-2008 was used to test the chemical stability (water resistance, acid resistance and alkali resistance) of the prepared pigments, and the results are shown in Figure 13, there is no obvious difference in the three types of filtrate or filter cakes. Under acidic conditions, the filtrate's pigment staining is rated 3–4, while the filter cake's discoloration is rated 5. Both staining and discoloration are at a highest level of 4 under alkaline conditions. This demonstrates the relatively outstanding acid and alkali resistance of the prepared pigment samples.
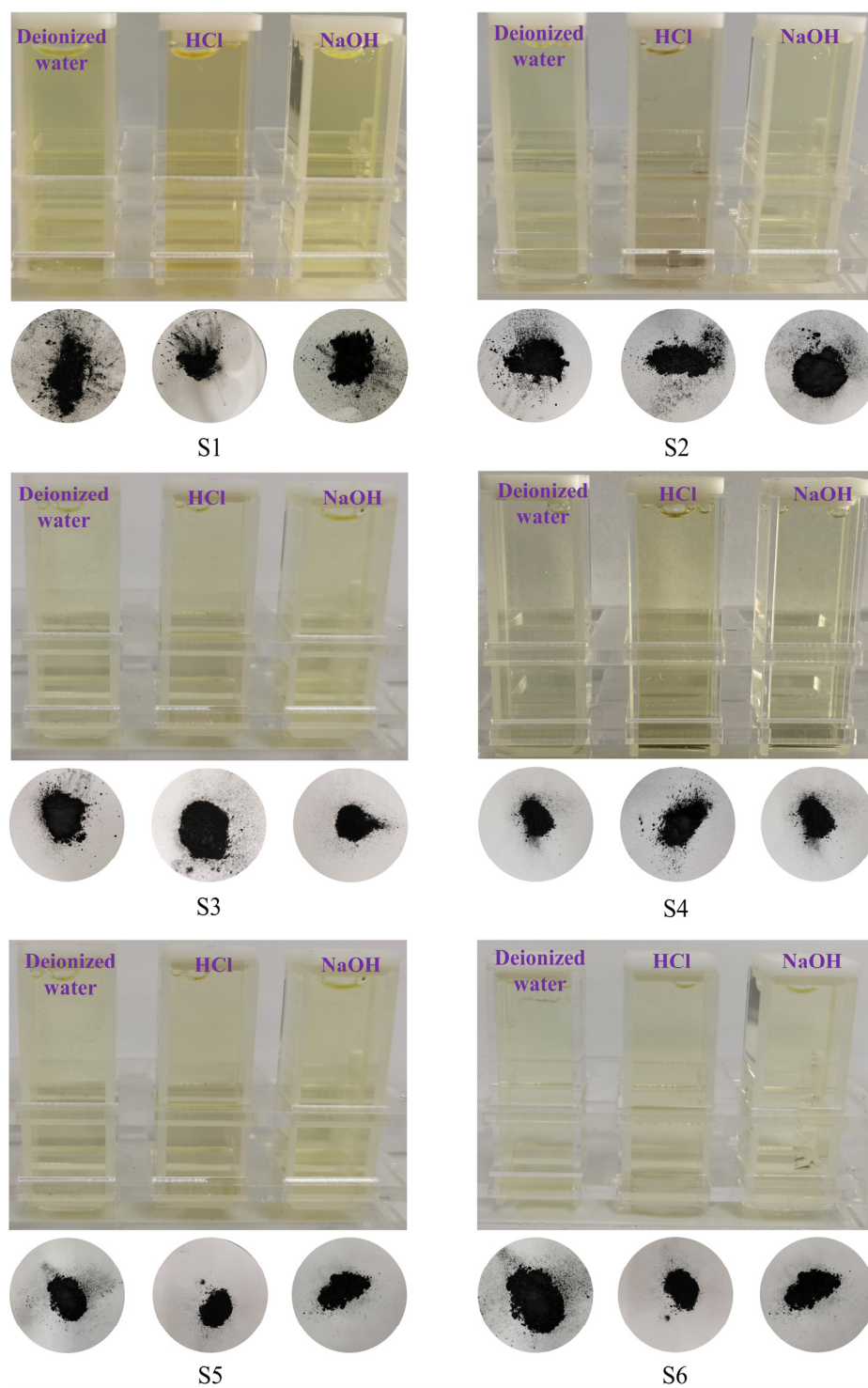

Figure 13. Filtrate and filter of prepared pigment samples.

3.8. Application Studies of the Prepared Pigments

Figure 14 exhibits the glazed surface for ceramic tiles prepared with various pigment samples. The glazed surfaces of ceramic tiles are black and crack-free, indicating that they have great adaptability with the transparent glaze. The *L**, *a** and *b** values of S1–S6 decrease from 41.8, 0.6, 1.6 to 32.0, 1.0 and 0.8, respectively, which shows excellent color rendering performance.

| Transparent glaze | S1 | S2 | S3 | S4 | S5 | S6 |

L* 73.1 *a** 0.4 *b** 7.8 | *L** 41.8 *a** 0.6 *b** 1.6 | *L** 39.8 *a** 0.4 *b** 0.3 | *L** 34.2 *a** 1.8 *b** 0.8 | *L** 33.4 *a** 1.7 *b** 1.0 | *L** 32.5 *a** 1.2 *b** 0.9 | *L** 32.0 *a** 1.0 *b** 0.8

Figure 14. Surface of glazed ceramic tiles.

4. Conclusions

(1) With the increase of MnO content in raw material, Mn gradually replaces Ni in the spinel phase, the average grain size becomes larger, the crystal plane spacing of black pigments increases from 0.2525 nm to 0.2535 nm, the grain size grows from 61.4619 nm to 79.7171 nm, and the lattice constant grows from 0.8377 to 0.8406 nm.

(2) With the increase of MnO in the Fe–Cr–Ni–Mn series of black pigments, Mn_3O_4, $MnCr_2O_4$ and $Ni(Fe,Cr)O_4$ begin to be generated, and exhibit a regular polyhedral structure. The band gap is reduced from 1.483 eV to 1.244 eV, the absorbance increases significantly and has a consistent absorbance in the visible range. Meanwhile, the *L**, *a**, and *b** values are reduced from 41.8, 0.6, 1.6 to 32.0, 1.0, 0.8, respectively.

(3) The Fe–Cr–Ni–Mn series of black pigments have great stability at 1100 °C, the best pigments in the Fe–Cr–Ni–Mn series of black pigments are chemically stable, acid, alkali and water resistant, with filtrate staining levels of 3–4 and higher, and cake discoloration levels of 5, which are sufficient for daily environments.

(4) The absorbance of prepared pigments is highly consistent. With the formation of Mn-containing spinel phases and the increase in the concentration of transition metals, resulting in a shift in band gap energy and an enhancement of UV–Vis absorption.

Author Contributions: The manuscript was written through contributions of all authors. M.L. and G.M.: Conceptualization, Investigation, and Supervision. X.Z. and Y.X.: Writing original draft and image processing. Y.X., T.D., Z.L. and R.H.: Validation, Resources, Investigation, Writing—review and Editing. M.L., X.Z. and G.M.: Verification and Modification. All authors have read and agreed to the published version of the manuscript.

Institutional Review Board Statement: Not applicable.

Informed Consent Statement: Not applicable.

Data Availability Statement: The authors confirm that the data of this study is contained within the article.

Conflicts of Interest: Author Zhiqiao Li was employed by the Pangang Group Research Institute Co., Ltd. The remaining authors declare that the research was conducted in the absence of any commercial or financial relationships that could be construed as a potential conflict of interest.

Abbreviations

SSD	Stainless Steel Dust
ICP-AES	Inductively Coupled Plasma-Atomic Emission Spectrometry
XRD	X-ray Diffraction Patterns

FTIR	Fourier Transform Infra-Red
UV–Vis	UV–Visible Spectrophotometer
SEM	Scanning Electron Microscopy
EDS	Energy Dispersion Spectrum
TG	Thermogravimetric
DSC	Differential Scanning Calorimetry

References

1. Zhou, Y.; Wang, H.Y.; Zhu, R.; Wei, G.S.; Dong, K. Green and efficient recovery of stainless steel dust by iron-bath direct reduction. *Sep. Purif. Technol.* **2023**, *308*, 123005. [CrossRef]
2. Liu, P.J.; Liu, Z.G.; Chu, M.S.; Yan, R.J.; Li, F.; Tang, J.; Feng, J.G. Detoxification and comprehensive recovery of stainless steel dust and chromium containing slag: Synergistic reduction mechanism and process parameter optimization. *Process Saf. Environ. Prot.* **2022**, *164*, 678–695. [CrossRef]
3. Liu, P.J.; Liu, Z.G.; Chu, M.S.; Yan, R.J.; Li, F.; Tang, J.; Feng, J.G. Multiobjective collaborative optimization of novel carbothermal reduction process of stainless steel dust and laterite nickel ore. *Trans. Nonferrous Met. Soc. China* **2023**, *33*, 1919–1931. [CrossRef]
4. Liu, P.J.; Liu, Z.G.; Chu, M.S.; Yan, R.J.; Li, F.; Tang, J. Silicate slag system in carbothermal reduction of stainless steel dust: Strengthening mechanism and stable regulation. *Mater. Chem. Phys.* **2023**, *304*, 127850. [CrossRef]
5. Ri, S.C.; Chu, M.S.; Chen, S.Y.; Liu, Z.G.; Hong, H. Self-reduction mechanism of coal composite stainless steel dust hot briquette. *J. Iron Steel Res. Int.* **2016**, *23*, 314–321. [CrossRef]
6. Liu, P.J.; Liu, Z.G.; Chu, M.S.; Yan, R.J.; Li, F.; Tang, J. Carbothermal reduction of stainless steel dust and laterite nickel ore: Slag phase behavior regulation and self-pulverization control mechanism. *ISIJ Int.* **2023**, *63*, 586–595. [CrossRef]
7. Zhuang, Q.Y.; Zhou, R.; Li, G.S.; Zhang, Y.H.; Xiong, X.L.; Geng, S.H.; Zou, X.L.; Cheng, H.W.; Zhang, Y.W.; Xu, Q.; et al. Synergistic preparation of metalized pellets using stainless-steel pickling sludge and blast-furnace bag dust. *Metall. Mater. Trans. B* **2022**, *53*, 1564–1582. [CrossRef]
8. Zhu, R.L.; Huang, R.; Xu, A.X.; Li, B.; Zang, Y.G.; Deng, X.; Yang, J.; Li, M.; Long, X.Z. Research status and development of extraction process of zinc-bearing dust from ironmaking and steelmaking—A critical review. *J. Iron Steel Res. Int.* **2023**, *30*, 1303–1323. [CrossRef]
9. Nemchinova, N.V.; Patrushov, A.E.; Tyutrin, A.A. Pyrometallurgical technology for extracting iron and zinc from electric arc furnace dust. *Appl. Sci.* **2023**, *13*, 6204. [CrossRef]
10. Shi, Z.S.; Ding, Y.J.; Yin, X.P.; Liu, B.; Shen, H.L.; Wu, B.Y.; Zhao, B.H.; Han, F.L.; Ekberg, C.; Zhang, S.G. Enrichment of Ni–Mo–V via pyrometallurgical reduction from spent hydrogenation catalysts and the multi-reaction mechanism. *Rare Met.* **2023**, *42*, 2700–2712. [CrossRef]
11. Lai, F.B.; Shi, W.; Hu, S.Y.; Li, X.H.; Chang, Q.B.; Wang, Y.Q.; Wang, Q.K. $SrMn_{1-x}Fe_xO_{3-\delta}$ (x = 0–1) black ceramic pigment: Synthesis, color properties, and application. *Ceram. Int.* **2023**, *49*, 28824–28836. [CrossRef]
12. Zhang, M.Q.; Yang, Y.J.; Feng, L.; Sun, X.Q. Synthesis and characterization of Fe^{3+} doped $YIn_{1-y}Mn_yO_3$ black pigment with high near-infrared reflectance. *Ceram. Int.* **2023**, *49*, 19290–19300. [CrossRef]
13. Hajjaji, W.; Zanelli, C.; Seabra, M.P.; Dondi, M.; Labrincha, J.A. Cr-doped titanite pigment based on industrial rejects. *Chem. Eng. J.* **2010**, *158*, 167–172. [CrossRef]
14. Dondi, M.; Zanelli, C.; Ardit, M.; Cruciani, G.; Mantovani, L.; Tribaudino, M.; Andreozzi, G.B. Ni–Free, black ceramic pigments based on Co—Cr—Fe—Mn spinels: A reappraisal of crystal structure, colour and technological behaviour. *Ceram. Int.* **2013**, *39*, 9533–9547. [CrossRef]
15. Liu, M.K.; Ma, G.J.; Zhang, X.; Zheng, D.L.; Li, Z.Q. Preparation and coloring mechanism of cobalt-free black ceramic pigments from stainless steelmaking dust. *Mater. Today Commun.* **2022**, *33*, 104609. [CrossRef]
16. Li, Z.Q.; Zhang, X.; Ma, G.J.; Muvunyi, R.A.; Zheng, D.L. Comparison of microwave and conventional processing stainless steelmaking dust to prepare black ceramic pigments. *J. Ceram. Process. Res.* **2023**, *24*, 1–7. [CrossRef]
17. Li, Z.Q.; Zhang, X.; Ma, G.J.; Zheng, D.L.; Xu, J.; Xu, J. Effect of the Fe/Cr molar ratio and calcination temperature on the preparation of black ceramic pigment with stainless steel dust assisted by microwave processing. *J. Clean. Prod.* **2022**, *372*, 133751. [CrossRef]
18. Li, Z.Q.; Zhang, X.; Ma, G.J.; Zheng, D.L.; Du, T.Y.; He, R.X. Effect of the nickel molar content on the preparation and properties of spinel-type black ceramic pigment by microwave processing from stainless steelmaking dust. *Mater. Today Commun.* **2022**, *32*, 104151. [CrossRef]
19. Singh, C.; Khanna, V.; Singh, S. Sustainability of microwave heating in materials processing technologies. *Mater. Today Proc.* **2023**, *73*, 241–248. [CrossRef]
20. García-Baños, B.; Sánchez, J.R.; Godes, J.L.; Leonelli, C.; Catalá-Civera, J.M. Evaluation of microwave synthesis of ceramic pigments based on in situ dielectric characterization. *Materials* **2023**, *16*, 2976. [CrossRef]
21. Singh, R.; Sharma, V.; Pandey, P.M. Microstructural characteristics and mechanical behaviour of microwave-assisted sintered novel WC-Co ceramic based internally cooled turning tool. *Mater. Charact.* **2023**, *200*, 112855. [CrossRef]

22. Wang, J.Y.; Han, A.J.; Ye, M.Q.; Chen, C.L.; Chen, X.; Zhu, X.F. Thermal insulation performance of novel coated fabrics based on Fe-Doped $BaSnO_3$ near-infrared reflectance pigments. *ACS Sustain. Chem. Eng.* **2021**, *9*, 16328–16337. [CrossRef]

23. Batista, G.H.; Psofogiannakis, G.; Junkermeier, C.E.; Paupitz, R. Mechanical properties and deformation-driven band gap tuning on [N]-Carbophenes. *Comput. Mater. Sci.* **2023**, *222*, 112103. [CrossRef]

24. Blasco-Zarzoso, S.; Beltrán-Mir, H.; Cordoncillo, E. Sustainable norganic pigments with high near-infra-red reflectance based on Fe^{3+} doped $YAlO_3$ for high temperature applications. *J. Alloys Compd.* **2023**, *960*, 170695. [CrossRef]

25. Dzurenda, L. Natural variability of the color of beech wood in the color space CIE *L*a*b**. *Forests* **2023**, *14*, 1103. [CrossRef]

26. Mu, P.Y.; Zhou, G.T.; Chen, L.C.; Zhang, Z.F.; Zhang, Y.W.; Shen, W.X.; Wang, Q.Q.; Wan, B.; Fang, C.; Jia, X.P. Effect of Ni_2O_3 on diamond crystal growth in an Fe–Ni–C system under high temperature and high pressure. *CrystEngComm* **2021**, *23*, 2809–2815. [CrossRef]

27. Sánchez-Ramos, S.; Doménech-Carbó, A.; Gimeno-Adelantado, J.V.; Peris-Vicente, J.; Valle-Algarra, F.M. Thermal Decomposition of Chromite Spinel with Chlorite Admixture. *Thermochim. Acta* **2008**, *476*, 11–19. [CrossRef]

28. Roy, R.; Dutta, A. Structural, optical, electrical, and dielectric relaxation properties of rare earth containing sodium bismuth Titanate $Na_{0.5}Bi_{0.5}TiO_3$ perovskite: Effect of ionic radius. *J. Rare Earths* **2023**. [CrossRef]

29. Gomaa, H.M.; Saudi, H.A.; Elkatlawy, S.M.; Yahia, I.S.; Makram, B.M.A.; Zahran, H.Y. Structure and electrical properties of some Fe-doped sodium borate devitrified glasses: Self-heating action. *Appl. Phys. A* **2023**, *129*, 322. [CrossRef]

30. Sadat, M.E.; Bud'ko, S.L.; Ewing, R.C.; Xu, H.; Pauletti, G.M.; Mast, D.B.; Shi, D.L. Effect of dipole interactions on blocking temperature and relaxation dynamics of superparamagnetic iron-oxide (Fe_3O_4) nanoparticle systems. *Materials* **2023**, *16*, 496. [CrossRef] [PubMed]

31. Gu, S.M.; Xia, M.; Zhou, C.; Kong, Z.H.; Molokeev, M.S.; Liu, L.; Wong, W.Y.; Zhou, Z. Red shift properties, crystal field theory and nephelauxetic effect on Mn^{4+}-doped $SrMgAl_{10-y}Ga_yO_{17}$ red phosphor for plant growth LED Light. *Chem. Eng. J.* **2020**, *396*, 125208. [CrossRef]

32. Ye, M.Y.; Zhou, Y.Y.; Shao, T.Y.; Liu, H.Z.; Tao, Q.; Wang, X.; Tang, R.L.; Yue, H.J.; Li, Y.; Zhu, P.W. Effects of high pressure on the bandgap and the d–d crystal field transitions in wolframite $NiWO_4$. *J. Phys. Chem. C* **2023**, *127*, 6543–6551. [CrossRef]

33. Kim, G.; Sohn, I. Selective metal cation concentration during the solidification of stainless steel EAF dust and slag mixtures from high temperatures for increased Cr recovery. *J. Hazard. Mater.* **2018**, *359*, 174–185. [CrossRef] [PubMed]

34. Khan, M.S.; Zou, B.S.; Shi, L.J.; Yao, S.F.; Bukhtiar, A.; Huang, W.G.; Lu, Y.; Cao, J.J.; Zheng, B.L. Carrier-mediated ferromagnetism in Mn(II)-doped ZnTe thin films and their optical properties: A first-principles study. *J. Alloys Compd.* **2023**, *964*, 171316. [CrossRef]

35. Khan, M.S.; Zou, B.S.; Yao, S.F.; Haq, Z.U.; Abdulla, A.S.; Huang, W.G.; Zheng, B.L. Suppression of ferromagnetism due to N Co-doping in Cr(II)-doped ZnS nanowires and their optical properties: Insights from density-functional calculations. *J. Magn. Magn. Mater.* **2023**, *582*, 171013. [CrossRef]

36. Thulasiramudu, A.; Buddhudu, S. Optical characterization of Mn^{2+}, Ni^{2+} and Co^{2+} ions doped zinc lead borate glasses. *J. Quant. Spectrosc. Radiat. Transf.* **2006**, *102*, 212–227. [CrossRef]

37. Charytanowicz, T.; Sieklucka, B.; Chorazy, S. Lanthanide hexacyanidoruthenate frameworks for multicolor to white-light emission realized by the combination of d-d, d-f, and f-f electronic transitions. *Inorg. Chem.* **2023**, *62*, 1611–1627. [CrossRef]

38. Qi, Y.J.; Qi, H.Y.; Li, J.H.; Lu, C.J. Synthesis, microstructures and UV–Vis absorption properties of β-$Ni(OH)_2$ nanoplates and NiO nanostructures. *J. Cryst. Growth* **2008**, *310*, 4221–4225. [CrossRef]

39. Pailhé, N.; Wattiaux, A.; Gaudon, M.; Demourgues, A. Correlation between structural features and Vis–NIR spectra of α-Fe_2O_3 hematite and AFe_2O_4 spinel oxides (A=Mg, Zn). *J. Solid State Chem.* **2008**, *181*, 1040–1047. [CrossRef]

40. Zhou, X.; Zhao, M.H.; Yang, J.; Han, Y.; Cao, L.; Han, Y.Y.; Wang, J.; Wang, Y.; Li, M.R. Chemical pressure enlarged camouflage color zone in Mn(IV)-activated yellow-green pigments. *Mater. Today Chem.* **2022**, *25*, 100902. [CrossRef]

41. Fang, P.; Zhou, S.Y.; Liu, Y.; Ye, J.Y.; Wang, L.Z.; Li, C.; Zhuo, S.; Chen, W.F. Solution combustion synthesis of gray-blue Mn-Doped YBO_3 pigments with high NIR reflectance for energy-saving buildings. *Ceram. Int.* **2022**, *48*, 37203–37211. [CrossRef]

42. Banik, S.; Samina, P.I.; Rao, P.N.; Srivastava, H.; Sagdeo, A. Probing interband and intraband transitions in magneto-optical FeT (T = Cr, Co, Ni) alloys from electronic structure studies. *Appl. Surf. Sci.* **2021**, *546*, 148896. [CrossRef]